Applied Catalysis B: Environmental 299 (2021) 120667

Contents lists available at ScienceDirect

Applied Catalysis B: Environmental

journal homepage: www.elsevier.com/locate/apcatb

Direct ammonia synthesis from the air via gliding arc plasma integrated with single atom electrocatalysis

Angjian Wu [a,1], Ji Yang [b,d,1], Bo Xu [c], Xiao-Yu Wu [e], Yuhang Wang [f], Xingjie Lv [a], Yichen Ma [g], Aoni Xu [a], Jiageng Zheng [a], Qinhuai Tan [a], Yaqi Peng [a], Zhifu Qi [a], Haifeng Qi [b], Jianfeng Li [d], Yaolin Wang [g], Jonathan Harding [g], Xin Tu [g], Aiqin Wang [b,*], Jianhua Yan [a,*], Xiaodong Li [a,*]

[a] State Key Laboratory of Clean Energy Utilization, Department of Energy engineering, Zhejiang University, Hangzhou, 310027, China
[b] State Key Laboratory of Catalysis, Collaborative Innovation Center of Chemistry for Energy Materials (iChEM), Dalian Institute of Chemical Physics, Chinese Academy of Sciences, Dalian 116023, China
[c] Department of Civil and Environmental Engineering, Washington State University, Pullman, WA 99164, USA
[d] State Key Laboratory for Physical Chemistry of Solid Surfaces, iChEM, College of Chemistry and Chemical Engineering, Xiamen University, Xiamen 361005, China
[e] Department of Mechanical and Mechatronics Engineering, University of Waterloo, ON N2L 3G1, Canada
[f] Institute of Functional Nano & Soft Materials (FUNSOM), Jiangsu Key Laboratory for Carbon-Based Functional Materials and Devices, Soochow University, Suzhou 215123, China
[g] Department of Electrical Engineering and Electronics, University of Liverpool, Liverpool L69 3GJ, UK

ARTICLE INFO

Keywords:
Ammonia synthesis
Plasma-electrocatalysis
Co single atom
Reaction mechanism

ABSTRACT

Industrial ammonia synthesis revolutionized global agriculture and industry, but it consumes significant amounts of energy and releases vast quantities of CO_2. One alternative, electrocatalytic nitrogen reduction generally suffers from a low ammonia yield rate and poor selectivity. Here, a tandem "plasma-electrocatalysis" strategy was proposed to harvest ammonia from the air. An ammonia yield rate (~1.43 mg_{NH3} cm^{-2} h^{-1}) with almost 100% faradaic efficiency was achieved during over 50 hours of stable operation at -0.33 V vs. RHE. The ammonia yield rate reached up to ~3.0 mg_{NH3} cm^{-2} h^{-1} with a faradaic efficiency of ~62% at -0.63 V vs. RHE. This marked performance is achieved by separating activation of stable nitrogen molecules via non-thermal plasma, followed by selective ammonia synthesis via a cobalt single-atom electrocatalyst. This strategy may rival the Haber-Bosch process and the aspirational electrochemical nitrogen reduction at a distributed small-size ammonia production based on a techno-economic analysis.

1. Introduction

Ammonia (NH_3), currently produced predominantly by the Haber-Bosch process (HBP), is a vital platform molecule for agriculture and industry [1,2]. High temperature and high pressure (> 450 °C, 150–350 atm), as well as large scale, concentrated infrastructures are prerequisite for HBP, which consumes approximately 2% of the world's annual energy supply [3–5]. Besides, HBP utilizes fossil fuel-derived hydrogen, resulting in ~400 million tons of CO_2 emissions per annum that accounts for 1.2% of the annual global carbon emissions [6–9]. As an attractive alternative 'greener' route, electrochemical nitrogen reduction reaction (ENRR) powered by renewable energy holds the promise of a carbon neutral (if the electricity is carbon free) and on-site small-scale NH_3 generation with much lower energy costs [10–14]. However, commercial implementation of ENRR is mainly plagued by its low activity and selectivity, due to the key challenges of activating the highly stable and low solubility N_2 molecule (N≡N, 948 kJ/mol) in aqueous electrolyte [15]. Moreover, the competing hydrogen evolution reaction (HER) also hampers ENRR, which usually occurs at the approximate potentials [16]. Recently, significant efforts have been devoted to the rational design and optimization of electrocatalysts for ENRR. Li et al. reported an NH_3 yield of 49.8 $ugh^{-1}mg^{-1}$ with a faradaic efficiency of 27.3% using a Sb/Nb_2CT_x-MXene catalyst [17]. Chu et al. introduced defects to the catalyst design (e.g., creating vacancies and atom-doping) to optimize adsorption of intermediates and reduce energy barrier [18,19]. Besides, interface engineering such as designing a MoS_2/C_3N_4

* Corresponding authors.
E-mail addresses: aqwang@dicp.ac.cn (A. Wang), yanjh@zju.edu.cn (J. Yan), lixd@zju.edu.cn (X. Li).
[1] These authors contributed equally to this work.

https://doi.org/10.1016/j.apcatb.2021.120667
Received 16 July 2021; Received in revised form 23 August 2021; Accepted 25 August 2021
Available online 28 August 2021

heterostructure was also applied to boost ENRR performance [20]. Notwithstanding, slight increase in activity still leads to a compromise of faradaic efficiency [21–23]. Furthermore, ubiquitous contaminants seriously interfere with the accuracy and reproducibility in experimental practices. The recent reported stories of 'false-success' of ENRR was basically caused by experimental and theoretical flaw, especially attributed to the overlooked problem of the nitrogen-containing contaminants [24,25]. Therefore, the direct ENRR leading commercial-viable NH_3 production still remains a grand challenge in contemporary research and development.

Non-thermal plasma (NTP), benefiting from the presence of unique non-thermal equilibrium character and rich active species, offers to break the stubborn N_2 bond and harvest reactive nitrogen species (RNS) under mild condition [26,27]. NTP can effectively overcome the high reaction barrier of N_2 activation correlated to ammonia synthesis scaling relations in ENRR via vibrational excitation [6,23]. Distinct from the conventional thermal process or thermal plasma-based nitrogen fixation (Birkeland-Eyde process, 3~4 MJ/mol N) [6], the major energy consumed by NTP is mainly used to create a highly chemical-reactive atmosphere rather than heating the surroundings. Similar to ENRR, NTP can be powered by renewable electricity allowing it to achieve net-zero emissions. Dependent on the types of redox RNS, the development of NTP-based nitrogen fixation is generally split into two directions (NH_3 and nitrogen oxides) [10,28–30]. Low NH_3 yield rate and energy efficiency remain the major practical obstacles for direct NTP-based NH_3 synthesis from N_2 and H_2 [6]. Just like conventional ENRR, using H_2 as the feedstock also makes $N_2 + H_2$ plasma catalysis unattractive. As for a typical air/H_2O plasma, long-lived RNS such as nitrous oxides (NO_x) and nitrate/nitrite (NO_3^-/NO_2^-), instead of NH_3, dominates the products of plasma-N_2 activation (Eq. (1)). In addition, NTP is theoretically assumed to have approximately a 2.5 times lower limit of power consumption (~0.2 MJ/mol N) than HBP (~0.48 MJ/mol N) in terms of NO_x generation route [26].

$$O_2 + N_2 \xrightarrow{\text{plasma}} NO_x + NO_x^- \quad (1)$$

In fact, these plasma induced nitrogen oxides are also considered as more reactive intermediates, which promises better reaction kinetics for NH_3 synthesis, with relatively low dissociation energy and better mass transportation in aqueous electrolytes [30,31]. By insightful understanding and rationally integrating NTP with ENRR, direct air-to-NH_3 conversion can be conceived, to address the dilemma of N_2 activation and NH_3 selectivity simultaneously from both aforementioned technologies. However, limited work has been reported so far. Kumari firstly proposed synergistic plasma-assisted ENRR with an NH_3 rate of 3.24 ug_{NH3} cm^{-2} h^{-1} from N_2 and water [32]. Hawtof et al. reported electrolytic-form plasma system to realize 100% Faradaic efficiency with 0.44 mg_{NH3} h^{-1} production from N_2 [21]. Even so, pure N_2 are still used as the precursor, which means N_2 separation from the air is required for this process, leading to a N_2 usage cost of about $900 per ton even for a small-scale ammonia production.

Herein, we demonstrate a tandem plasma-electrocatalytic process to combine NTP with the conventional electrocatalysis for the highly efficient production of NH_3 directly from the air (Fig. 1). A warm plasma (gliding arc) was employed to convert air into NO_x followed by the electrocatalytic reduction of NO_x into NH_3. Single-atom catalysts with the unique electronic characteristics of isolated active sites were employed to improve the proton/electron transfer to the active sites and suppress HER [33–35]. Relying on this strategy and technology portfolio, we achieved an NH_3 yield rate of 1.43 ± 0.05 mg_{NH3} cm^{-2} h^{-1} (1430 ± 50 mg_{NH3} $h^{-1}g_{cat}^{-1}$), a faradaic efficiency of $98 \pm 0.7\%$ at -0.33 V vs. RHE, and 50-hour operating stability with a nearly constant NH_3 selectivity. The productivity and selectivity approach the U. S. DOE targets for commercial-viable NH_3 production (NH_3 yield rate of ~10^{-4} mole cm^{-2} h^{-1} and faradaic efficiency > 90%) [11,36]. Compared to HBP or ENRR, small-scale NH_3 synthesis (< 100 kg/h) by the integrated plasma-electrocatalysis is economically and environmentally available under the baseline industrial electricity price at $60/MWh. Without air separation units and fossil-based pure hydrogen production, the integrated plasma-electrocatalysis has great potential to contribute to the sustainable and distributed on-site ammonia production in remote areas and developing countries.

2. Experimental section

2.1. Preparation of Co single atom catalyst (Co SAs/N-C)

For a typical synthesis process, 30 g silica (40 wt.%) was added into a beaker, together with 400 mL H_2O and 5.45 g 2,6-Diaminopyridine. The mixture solution was vigorously stirred in ice bath for 2 h. Then, 1 g NaOH was added into the above mixture, and stirred for 10 min before the addition of 17.13 g/100 mL $(NH_4)_2S_2O_8$ aqueous solution. The obtained solution was stirred fiercely for 12 h, followed by sonication for 5 min, filtered and washed for several times with ultra-pure H_2O. After drying in the oven for 12 h at 80 °C, the nitrogen doped carbon (N-C) was obtained by calcining the powder at 800 °C for 2 h with a heating rate of 5 °C/min in NH_3 atmosphere, followed by etching with HF (5 vol. %). Eventually, 8 mg $Co(NO_3)_2{\cdot}6H_2O$ was dissolved into 50 ml ethanol and sonicated for 5 min with 100 mg the aforementioned prepared N-C. After stirring at room temperature for 12 h, the mixture was then filtered and dried under vacuum at 60 °C for 12 h, to obtain the Co SAs/N-C.

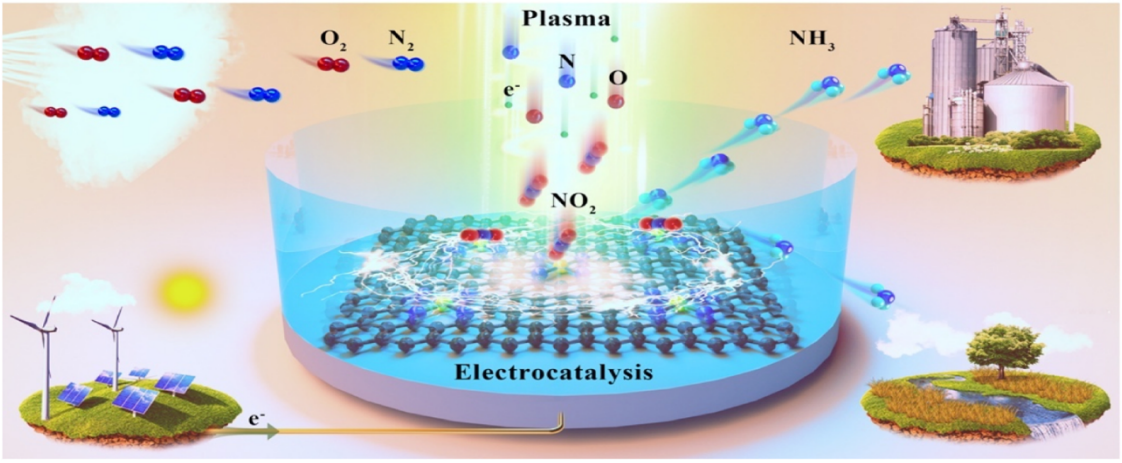

Fig. 1. Schematic illustration of plasma-electrocatalysis system for NH_3 synthesis. Powered by intermittent renewable electricity, air plasma can be integrated with an electrochemical system to directly harvest NH_3 from the air and water.

2.2. The Atmospheric rotating gliding arc plasma jet system

The atmosphere-pressure air plasma jet system mainly consisted of a home-made rotating gliding arc plasma jet reactor, feeding gas, mass flow controllers (MFCs, Sevenstar, D07 series), a DC power supply (Teslaman TLP 2040) and current-limiting resistor. The rotating gliding arc plasma jet reactor was made of stainless steel, with a cylinder-shaped anode (outer diameter of 10 mm, height of 80 mm) inserted a cylindrical cathode, the detailed geometric parameters was illustrated in Fig. S1. The narrowest gap between two electrodes was 3 mm, while the largest gap between two electrodes was 5 mm. The non-thermal plasma was ignited inside the cavity and blow through a nozzle design outlet by gas flow. Mixture of O_2 (99.99%) and N_2 (99.99%), and air was selected as the reactants, respectively. The electrical signals of the plasma jet in operation were recorded using a digital oscilloscope (Tektronix DPO4034B), while gas products were measured via a gas analyzer (MGA-5). The OES system, with a focal length of 750 mm monochromator (PI-Acton 2750 , 1e1400 nm, resolution 0.03 nm), optical fibers, liquid nitrogen cooled ICCD (PI-MAX 2, 512 × 512 pixel), was applied to identify the active species and also used to analyze the typical molecular vibrational-rotational bands and electronic transition.

2.3. Characterization of Co SAs/N-C catalysts

The scanning electron microscopy (SEM) was acquired on Zeiss Sigma 500 with the voltage of 10 kV. The transmission electron microscopy (TEM) and elemental mapping was performed on JEOL JEM-2100F with the accelerating voltage of 200 kV. HAADF-STEM image was characterized by Aberration-corrected high-angle annular dark-field scanning electron microscopy via a JEOL JEM-ARM200F STEM/TEM with a guaranteed resolution of 0.08 nm. X-ray photoelectron spectroscopy (XPS) was performed on a Thermo ESCALAB 250Xi spectrometer using Al Kα irradiation (Al Kα = 1846.6 eV), which was operated at 15 kV and 10.8 mA. X-ray diffraction (XRD) measurement was carried out on a PANalytical X'pert diffractometer using nickel-filtered Cu Kα radiation with a scanning angle (2θ) of 10°~90°. The Co loading weight was determined with inductively coupled plasma optical emission spectroscopy (ICP-OES) on an Optima 7300 DV instrument (PerkinElmer Corp.). Raman spectra was obtained using Labor Raman HR-800 with a laser excitation at 514 nm. Nitrogen sorption isotherms was obtained at -196 °C on a Quadrasorb SI (Automate Surface Area & Pore Size Analyzer, Quantachrome). The X-ray absorption spectra (XAS) measurements include X-ray absorption near-edge structure (XANES) and extended X-ray absorption fine structure (EXAFS) at the Co K-edge of Co SAs/N-C, which was performed at the 1W1B station in Beijing Syngchrontron Radiation Faciliy (BSRF), China.

2.4. Measurement of ammonia synthesis via Plasma-electrocatalysis

In a typical reaction process, 0.1 M KOH electrolyte was prepared in a glass reaction vessel and purged by Ar (99.99%) for 30 mins, followed by plasma treatment for 10 mins using air or N_2/O_2 mixture as the reactant. After that, 50 mL of plasma-treated electrolyte was transferred to a half cell of a conventional H-type cell for NH_3 synthesis, with cathode and anode separated by a Nafion membrane. The electrocatalysis was performed with a CHI 660 electrochemical workstation, using a platinum plate as the counter electrode, Ag/AgCl equipped with a salt bridge as the reference electrode, and a carbon paper (1 × 1 cm^2) with Co SAs/N-C catalysts load of 1 mg_{cat}/cm^2 as a working electrode. The quantification of generated NH_3 was spectrophotometrically determined using the widely indophenol blue method and compared with Nessler's regent, while the NH_3 yield rate was calculated via the following equation: $\boldsymbol{Y_{NH3} = c_{NH3} \times V/t}$. where $\boldsymbol{Y_{NH3}}$ denoted the NH_3 yield rate,. represented measured NH_3 concentration, V and t signified electrolyte volume and electrocatalytic time, respectively. Faradaic efficiency (FE) was defined as the charge consumed for ammonia synthesis, divided by the total charge passing through the electrolytic system. Herein, FE was calculated via the following equation based on the practical electrocatalytic conversion from plasma-induced products in electrolyte to NH_3: $\mathbf{FE}(\%) = (\boldsymbol{n_e} \times \boldsymbol{F} \times 100\%)/\boldsymbol{Q_T}$, where $\boldsymbol{n_e}$ denoted the total charge required to generated NH_3, F represented Faraday constant (96485 C mol^{-1}), $\boldsymbol{Q_T}$ was the quantity of charge integrated by the i-t curve. To trace and confirm nitrogen source, isotope labelling experiment was designed and performed using ^1H NMR (600 MHz, Agilent Technologies). In addition, the liquid product in plasma-treated electrolyte was quantified by ion chromatography (IC) before and after the electrocatalytic process. The detail information was provided in Supplementary Msaterials.

2.5. Computational simulation and techno-economic assessment

COMSOL Multiphysics software was used to develop a 3D fluid model to intuitively reflect the sophisticated physio-chemical processes induced by non-thermal plasma, with the consideration of the mutual interactions amongst fluid field, temperature field, electric field and plasma chemistry. Part of boundary conditions were listed as follows: applied voltage of 10 kV; gas flow rate of 7 L/min; plasma-electrolyte distance of 1 cm; initial temperature of 300 K; initial pressure of 1 atm. In terms of the plasma activation, 36 key species and 74 steps elementary reactions were considered. As for electrocatalysis, Density functional theory (DFT) [37] calculations were performed using the method encoded in the Quantum ESPRESSO software package, to further reveal the NH_3 synthesis at the interface of Co single atom catalysts [38]. The local density approximation (LDA) functional was used for the exchange-correlation energy [39] and norm-conserving Troullier-Martins type pseudopotentials were used in place of the all electron atomic potentials [40]. The wave function was expressed as a plane-wave summation truncated at an energy cutoff of 1020 eV and Kohn-Sham energies were sampled across the Brillouin zone using a 4×4×1 Monkhorst-Pack grid [41] to ensure that the calculated forces are converged to better than 5 meV/Å. In the Co SAc/N-C structural model, Co atoms connected with four N atoms, consistent with the results from EXAFS. The planar surface with total of 144 atoms were used in all calculations.

A techno-economic analysis (TEA) was performed to identify the profitable NH_3 manufacturing and compare the Levelized cost of NH_3 (LCOA) with electrified HBP and ENRR. For H_2O electrolyzer + air separation unit + HB reactor (HBP) and the electrochemical nitrogen reduction + air separation unit (ENRR) technologies, the state-of-the-art performances reported in reference was used for the evaluation [42]. The electricity cost for the base study was $60/MWh. Both capital costs (CAPEX) and operation costs were considered, while the energy consumption of plasma-electrocatalysis mainly derived from both plasma part and electrocatalysis part from experimental measurements. More detail information was provided in Supplementary Materials.

3. Results and discussion

3.1. Design of a tandem plasma-electrocatalysis system for air-to-NH_3

To realize this "plasma-electrocatalysis" strategy, rotating gliding arc plasma jet was applied as the first step to produce RNS directly from the ubiquitous air (Fig. 2A). Compared with other types of NTPs for NO_x production (such as dielectric barrier discharge, corona discharge, glow discharge, etc.,), rotating gliding arc plasma has the prominent advantages of a relatively low energy cost (< 5 MJ/mol N) and a reasonable processing capacity (2–20 L/min) [28,43,44]. Such energy cost was much lower than Sun et al., which harvested NO_x intermediaries at energy cost of ~14 MJ/mol N using liquid-discharge [45]. To optimizing NTP treatment, the effect of operating parameters was revealed by both experiments and simulation, with the consideration of the complexity of multi-physiochemical fields coupled in the NTP system

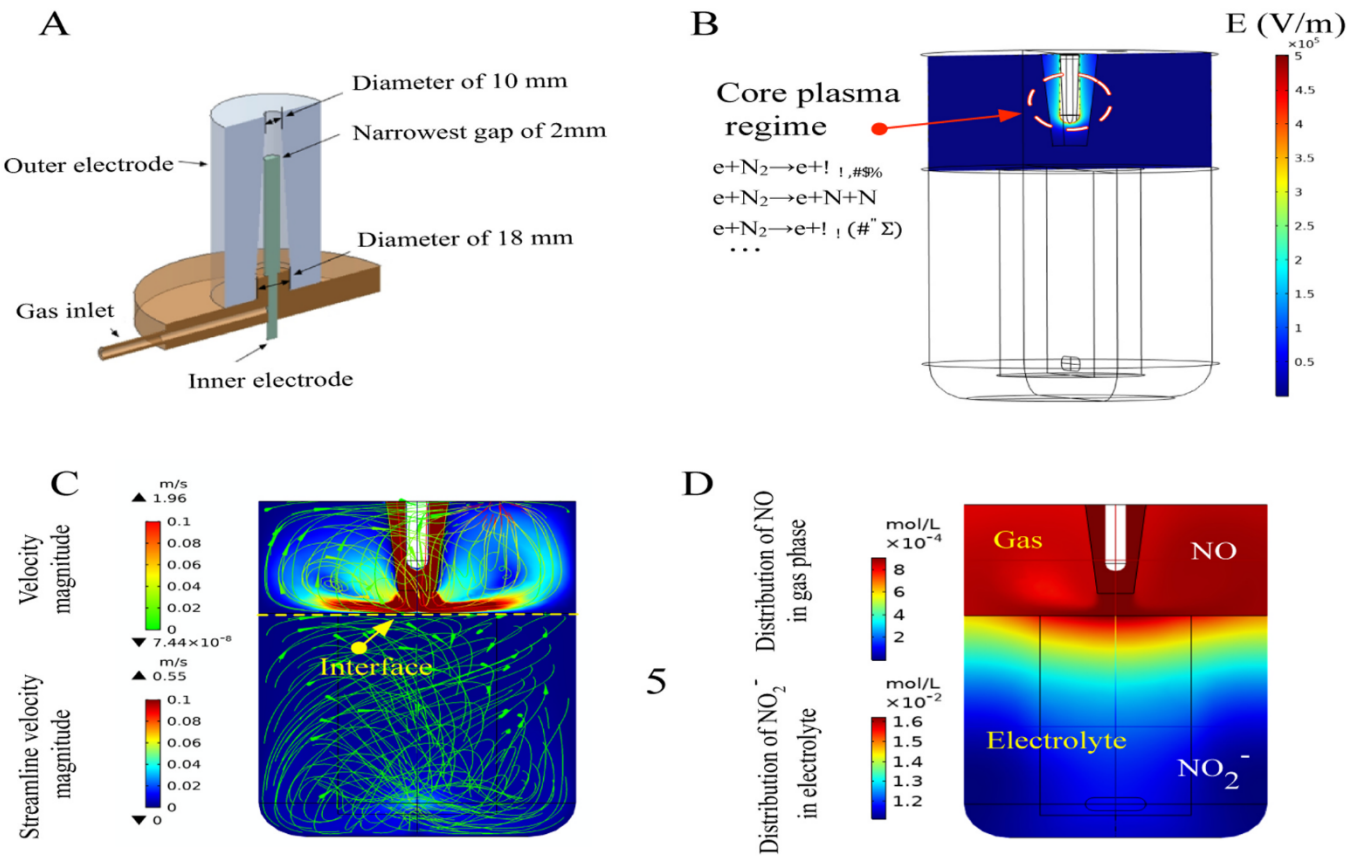

Fig. 2. (A) Design of rotating gliding arc plasma jet; Distribution of (B) electric filed, (C) velocity field in NTP and distribution of NO and NO_2^- concentration.

(Figs. S1 and S2). In the previous work, NO_x concentration and energy consumption was greatly affected by applied voltage of the rotating gliding arc, due to the variation of the specific energy input in NTP [43]. The applied voltages tuned the distribution of electric field strength, which directly affect the electron-impact reactions in the vicinity of the inner electrode (Fig. 2B). With the enhancement of applied voltage, the NO_x^- concentration in the electrolyte increased linearly based on IC tests (Fig. S26-C). The joint effect of applied voltage and gas flow rate contributed to the distribution of plasma temperature. The significantly drop of plasma temperature along the axial and radial direction (Fig. S5), confirmed the fast transformation of plasma characteristics from thermal equilibrium into highly non-thermal equilibrium in our system [46]. It was worth noting the non-electron-initiated reactions such as neutral atoms-molecules reactions and radical-radical interactions were related to the temperature distribution and conformed to Arrhenius-type kinetics. The distance between plasma and electrolyte was also a key parameter in present work for the formed NO_x^- yield. With a narrower distance between the plasma jet and electrolyte, an 8-fold increase in NO_2^- concentration was observed via IC tests (Fig. S26-A). According to the simulation, the velocity field distribution was determined by plasma-electrolyte distance and gas flow rate, while in turn affected the air discharge and transportation of plasma-induced species (Figs. 2C and S3). Rigorous stirring accelerated the diffusion and reaction of the hydrophilic RNS from the plasma phase to the liquid phase (Fig. S4). Thus, by agile adjustment of the operating parameters, the performance of NTP treatment as well as the distribution and transportation of NTP induced RNS in the gas/liquid-phase was eventually determined by the collective effect of multi-physical fields in rotating gliding arc (Figs. 2D and S6).

Subsequently, a customized three-electrode H-type cell systemwas used to conduct NH_3 synthesis from plasma-induced NO_x intermediaries (Fig. 3A). We began by preparing the carbon nano-frame-confined N-coordinated Co single atom (Co SAs/N-C) via a facile metal-adsorbing strategy. Transmission electron microscopy (TEM) images demonstrated the Co SAs/N-C was porous and interweaved by curved fringes of the layered carbon (Fig. 3B). The catalyst has a Brunauer-Emmett-Teller (BET) surface area of 1256 m^2/g and an average mesoporous pore size of 10~20 nm (Fig. S7). Raman spectroscopy exhibited two featured peaks (D peak~1350 cm^{-1} and G peak ~1580 cm^{-1}) with a high ratio of intensity D to G peak, indicating the highly disorder or defect-rich structure of Co SAs/N-C after pyrolysis (Fig. S8). Aberration-corrected high-angle annular dark-field scanning electron microscopy (HAADF-STEM) and magnified HAADF-STEM images showed the isolated Co atoms were uniformly distributed, and no cluster and nanoparticles were detected in the vicinity of Co atoms [47,48] (Fig. 1C). The corresponding energy-dispersive X-ray spectroscopy (EDS) elemental mapping exhibits the homogeneous distribution of Co, C and N throughout the whole structure (Fig. S9). The X-ray power diffraction (XRD) patterns of Co SAs/N-C exhibits two broad characteristic graphitic peaks (002) and (101), while no peaks of Co-containing crystal particles are detected, which also implies highly dispersed Co SAs (Fig. S10). Using inductively coupled plasma optical emission spectroscopy (ICP-OES), we confirmed the mass loading of Co was ~1.1 wt%.

X-ray photoelectron (XPS) and X-ray absorption spectroscopies were used to further reveal the electronic and coordination structure of the Co sites at the atomic level. We found the pyridinic N-cobalt coordination structure of Co SAs/N-C (Figs. S11–S13 and 3D–G). The N1s spectra of Co SAs/N-C featured a new signal with a binding energy of 398.8 eV (purple shadow), which can be assigned to pyridinic-cobalt moieties (Fig. 3D) [49]. The X-ray near-edge structure (XANES) profile of Co SAs/N-C was relatively smooth, different from those reference samples. Besides, it exhibited a pre-edge peak located at ~7709 eV (1s→3d transition) arising from the oxygen-adsorbed Co structure (Fig. 3E). The absorption edge position positively shifted by 1 eV compared to that of

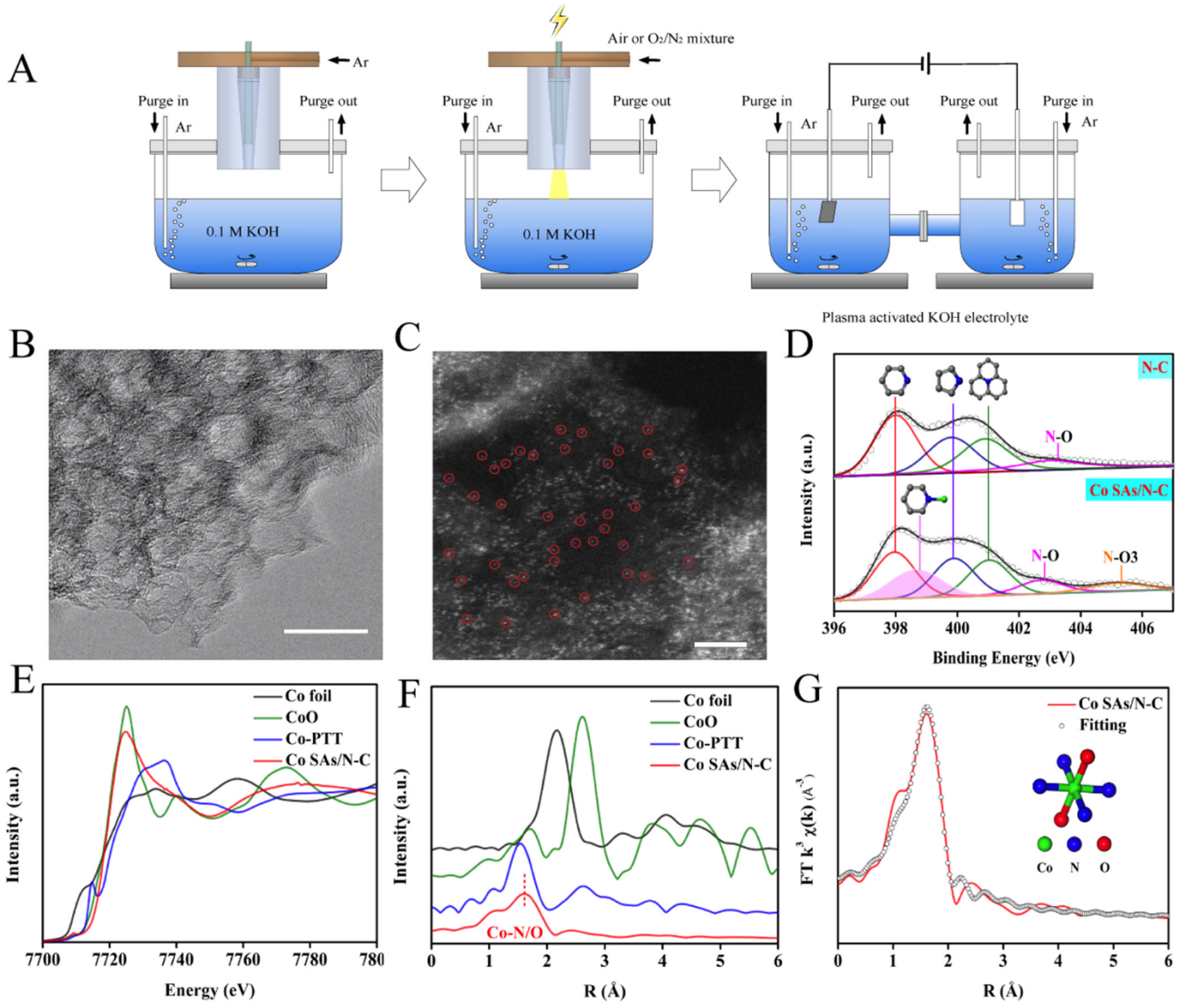

Fig. 3. (A) Scheme of tandem NTP-electrocatalysis for NH_3 synthesis from air mode. (B) HR-TEM image of Co SAs/N-C. Scale bars: 20 nm. (C) A HAADF-STEM image of Co SAs/N-C catalysts, scale bar: 2 nm. (D) The N1s XPS spectra of N-C and Co SAs/N-C catalysts. (E) The Co K-edge XANES profile and (F) the Co K-edge k^2-weighted FT-EXAFS in R space of Co SAs/N-C catalysts and reference samples including Co foil, CoO and Co-porphyrin (Co-PTT). (G) Corresponding EXAFS fitting curves at R space.

CoO, suggesting the valence state of Co species in Co SAs/N-C was slightly higher than +2. The Fourier-transformed k^2-weighted extended X-ray absorption fine structure (EXAFS) spectra for Co SAs/N-C exhibited only one peak within 1.5-1.7 Å, while no peaks at the position of Co-Co coordination were observed, which further confirms the absence of metallic Co or Co_x species (Fig. 3F) [50]. The best-fit analysis of EXAFS data in R-space (Fig. 1G) and k-space (Fig. S13) confirmed a 6-fold coordination structure of Co SAs/N-C mainly comprised of Co-N and Co-O bonds in the first coordination shell. According to the architectural model illustrated in the inset image (Fig. 3G), the fitted nitrogen-cobalt coordination number was about 4 (Table S1). Two axial oxygen atoms on the Co centers can be ascribed to weakly adsorbed oxygen species (e.g., O_2). Noting that the C1s XPS and O1s XPS spectra of Co SAs/N-C was almost the same as that of N-C, the results exclude the existence of surface carbon- and oxygen-defect-ligated Co sites (Fig. S12).

3.2. Activity evaluation of a tandem plasma-electrocatalysis for air-to-NH_3

The indophenol blue method was applied to quantitatively evaluate the NH_3 yield in this work, while Nessler's reagent method was also compared to exclude the effect of interferants on the quantification method [51]. Due to the relatively high concentration of the NH_3 yield, a series of 1000 μg/L ammonia standard solution was prepared to explore the influence of PH and methods on NH_3 detection. The indophenol blue method exhibited change sensitive to PH and was highly inaccurate in acidic solution due to the instability of NaOCl (Fig. S14). In terms of neutral and alkaline conditions, both methods exhibited similar accuracy at the given PH used in our experiments, which confirmed the feasibility of the indophenol blue method (Fig. S15). Furthermore, NMR tests also helped independently confirm the accuracy of results from indophenol blue method (Fig. S18). In present work, no sacrificial agents like alcohols and metal ions were detected to affect the measurement.

To further exclude the influence of other potential N sources, including nitrogen-containing materials or background gas

contamination, we used plasma-free and N-free control tests (Fig. 4A). Here, N_2 and air were comparatively used as feedstocks, while Ar was used as purge gas during the whole process via gas bubbling. Without plasma, or with only Ar present in process, no NH_3 was observed. When plasma was present with N_2 and air as the feedstocks, high yield of NH_3 was produced. Besides, air-plasma exhibited superior activity over N_2-plasma, which implied the key role of oxygen-containing RNS formed accounting for the subsequent integration with electrocatalysis. To verify that the air is the sole N source for NH_3 synthesis, isotope labelling experiment was performed by two specific designed experiments using ^1H NMR. Firstly, using the simulated air containing $^{15}N_2$ (100 mL/min) and Ar gas with a total flow rate of 7 L/min, we observed the formation of $^{15}NH_3$ with a typical double peak (Fig. 4B), while only a typical triple peak was observed with air as reactant. As ^{15}N-N_2 was stored in 1 L bag, continuous discharge with a large gas flow rate inevitably mixed with surrounding gas, which leaded to $^{14}NH_4^+$ peaks observed in ^{15}N-N_2 isotopic tracer test. By quantifying the gas- and liquid-product distribution after plasma activation, we pinpointed that NO_2^- was the species that bridges plasma and electrocatalysis (Fig. 2B). Similar to other reported work, NO_2^- was prone to be generated rather than NO_3^- in gas-liquid discharge in gliding arc plasma [52]. Then, we prepared ^{15}N-NO_2^- solution with a concentration of 0.015 mol/L according to the IC test after plasma activation. The mass balance of ^{15}N-containing species before and after electrolysis further validated the air-to-NH_3 conversion route in our plasma-electrocatalysis strategy (Figs. 4D and S16).

Then, we tested the impacts of various operating parameters on the performance of NH_3 synthesis. The NH_3 faradaic efficiency was herein evaluated in terms of nitrite reduction reaction process based on the previous product analysis. With a narrower distance between the plasma jet and electrolyte, the NH_3 yield rate increased drastically from 0.096 ± 0.02 to 1.43 ± 0.05 mg_{NH3} cm^{-2} h^{-1}, and the NH_3 faradaic efficiency rose from ~47% to ~98% (Fig. 5A). Faradaic efficiency remained above 90% at all the applied voltages and gas flow rates tested, while the NH_3 yield rate was doubled when the applied voltage increased from 6 kV to 10 kV (Fig. 5B and C). This could be due to the higher applied voltage and longer residence time both facilitating the formation of energetic electrons and active species for air activation and promoting the RNS generation. NH_3 yield rate and faradaic efficiency exhibited volcano-type relationships with the N_2/O_2 ratios in the feedstock (Fig. 5D), of which air exhibited the superior performance compared with other N_2/O_2 ratios. The similar variation tendencies of NO_2^- concentration and NH_3 yield rate under various operating conditions of NTP (such as applied voltage, plasma-electrolyte distance and gas types) was also observed, which further implied the important role of formed dissolved NO_2^- via rotating gliding arc for the subsequent electrocatalysis (Fig. S26). The effect of the potential on the electrocatalytic step was also investigated. The faradaic efficiency remained above 95% whilst positively shifting the potential to -0.13 V vs. RHE, while NH_3 yield rate decreased drastically to ~0.63 mg_{NH3} cm^{-2} h^{-1} in contrast. By shifting the potential to -0.63 V vs. RHE, the NH_3 yield rate approached ~3.0 mg_{NH3} cm^{-2} h^{-1} with the faradaic efficiency decreased to ~62% (Fig. 6A). To evaluate the system's stability for long-term operation, we performed an Air-to-NH_3 conversion at -0.33 V vs. RHE. An NH_3 yield rate of ~1.43 mg_{NH3} cm^{-2} h^{-1} (~1430 mg_{NH3} h^{-1} g_{cat}^{-1}) was achieved at a near-unity faradaic efficiency at a Co SAs/N-C catalyst load

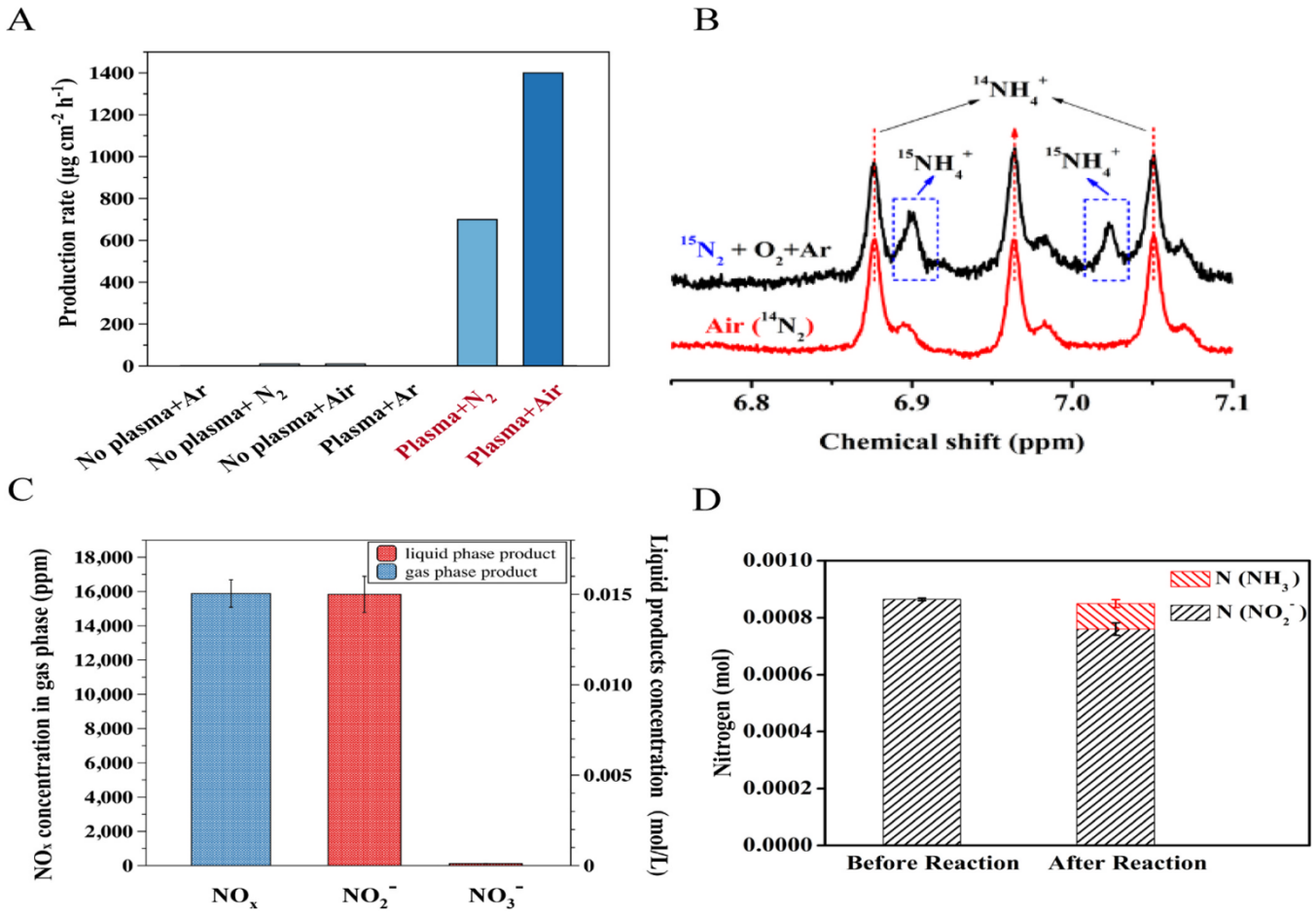

Fig. 4. (A) NH_3 yield rates for various gases and controls at -0.33 V vs. RHE after 10 mins electroreduction in 0.1 M KOH. (B) NMR test of N source via simulated air discharge (C) Products distribution in gas- and liquid- phase after air plasma treatment for 10 mins; (D) The mass balance of N-15 before and after electrocatalysis.

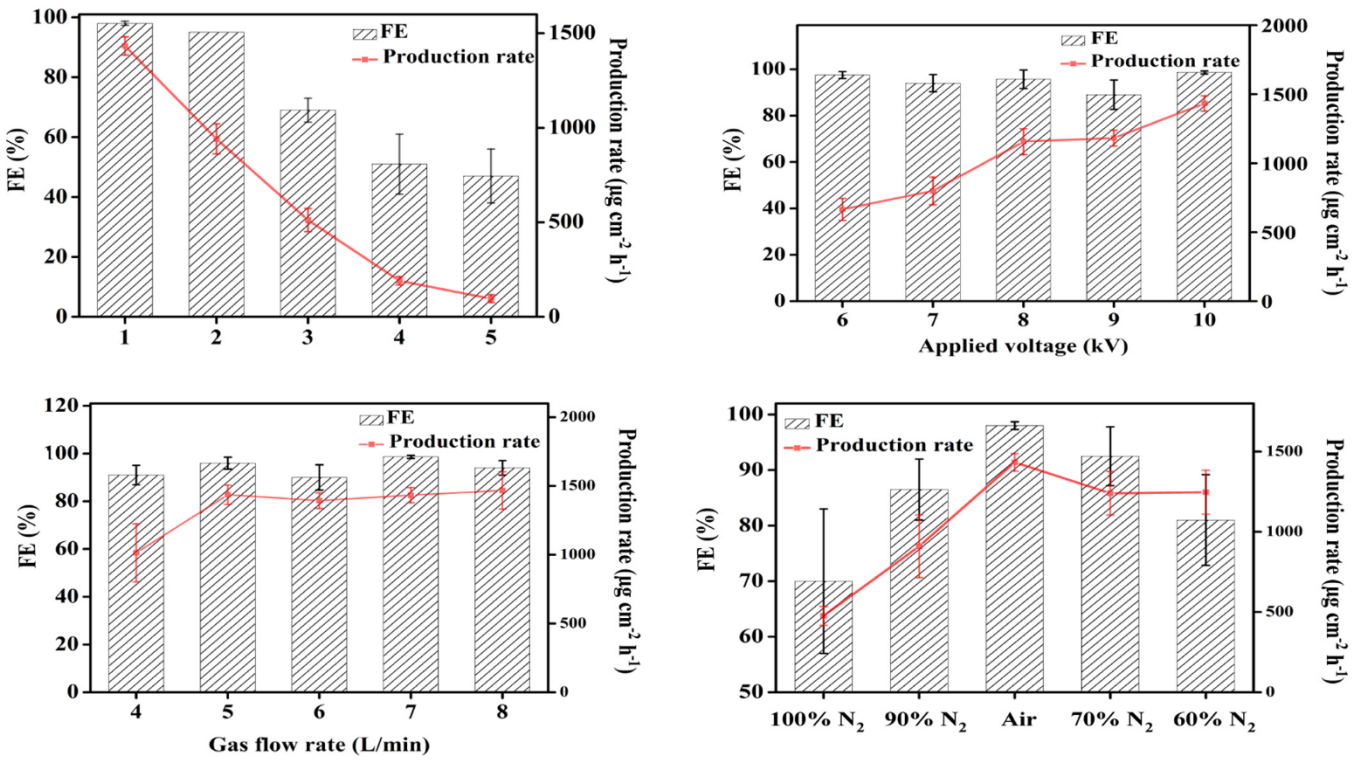

Fig. 5. NH_3 production activity based on the plasma-electrocatalysis strategy. Effects of (A) distance between the plasma jet and electrolyte, (B) applied voltage, (C) gas flow rate, and (D) N_2/O_2 ratio on NH_3 yield rate and faradaic efficiency at -0.33 V vs. RHE.

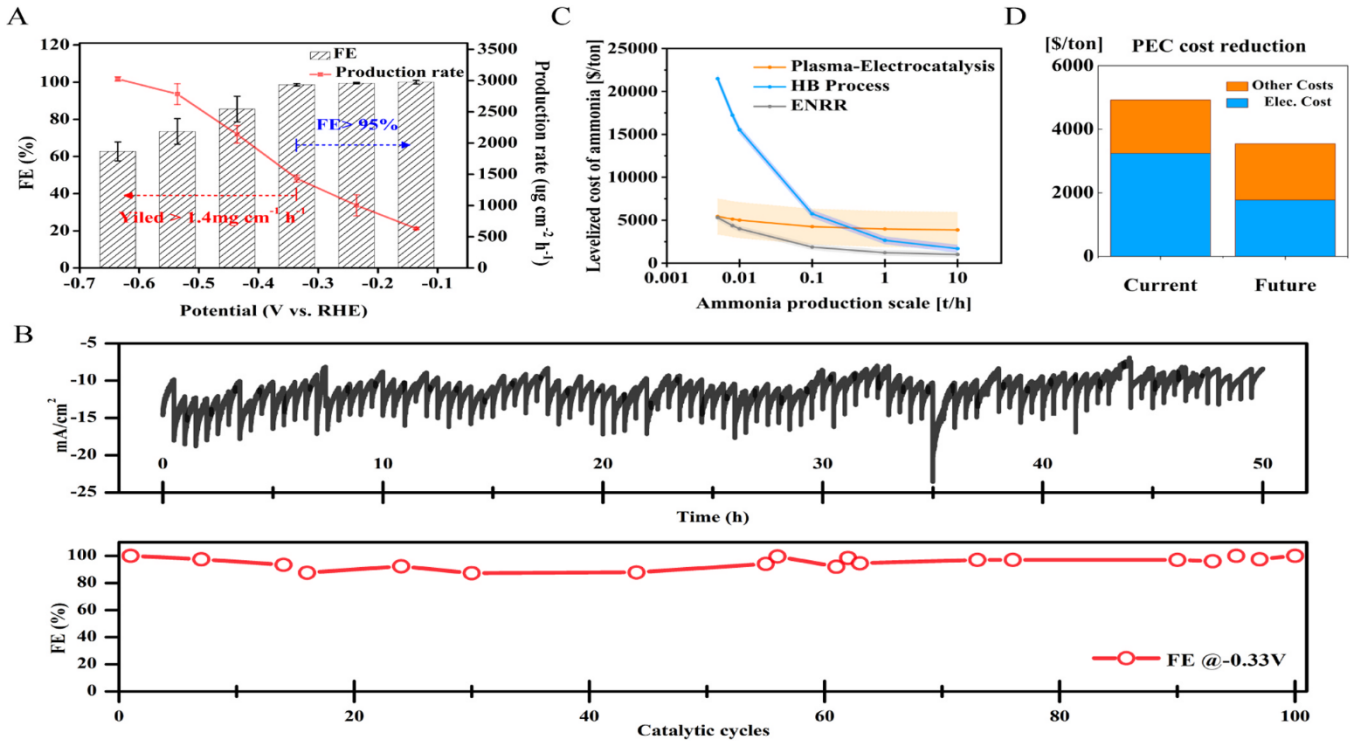

Fig. 6. NH_3 production stability and techno-economic assessment. (A) NH_3 yield rate and faradaic efficiency at different potentials (Plasma-electrolyte distance of 1 cm, a gas flow rate of 7 L/min, an applied voltage of 10 kV). (B) Chronoamperometry curve and faradaic efficiency of NH_3 synthesis at -0.33 V vs. RHE. (C) Techno-economic comparison of plasma-electrocatalysis strategy, HBP, and ENRR. (D) LCOA reduction of plasma-electrocatalysis strategy (0.01t/h) by optimizing operating conditions.

of 1 mg_{cat}/cm^2. Total current density and faradaic efficiency were remained almost constant for 100 runs a total duration of 50 hours (Fig. 6B). STEM and HAADF-STEM characterization of Co SAs/N-C revealed a slight aggregation of Co species might occur after the long-term operation, while a high density and relatively homogeneous dispersed Co single atoms was still retained (Fig. S19).

NH_3 production activity reported here outperformed previous N_2-to-NH_3 conversion over various state-of-the-art electrocatalysts (Fig. S20 and Table S3), due to different reaction pathway and kinetic energy barriers. In previous research, the NH_3 Faradaic efficiency is typically below 15%, and the productivity is far lower than the U. S. DOE target (10^{-4} mole cm^{-2} h^{-1}) [22,53–55]. For a benchmarking performance comparison, the energy consumption of our electrolyzer is 11.9 MWh/t-NH_3 in the best-scenario, which is close to an aspirational ENRR consumption of 8.64 MWh/t-NH_3 at 95% faradaic efficiency and 0.6 V overpotential [56]. In addition, the energy consumption of our plasma NO_x synthesis process was only about 2.4 MJ/mole N, better than that using other plasma systems [28,45,57] in terms of N_2-to-NO_x conversion (Table S4). Taking the energy used in the plasma reactor into consideration (Fig. S29), the total energy consumption of the plasma-electrocatalysis approaches 51.8 MWh/t-NH_3. A techno-economic analysis (TEA) was performed to identify the profitable NH_3 manufacturing and compare the Levelized cost of NH_3 (LCOA) with electrified HBP and ENRR (Tables S5–S7). For distributed NH_3 production with scales lower than 100 kg/h, the plasma-electrocatalysis strategy is more cost-effective than HBP at the baseline industrial electricity price of $60/MWh. We anticipate that our approach could lead to a breakeven NH_3 production cost to HBP at an electricity price of $20/MWh and a production scale of 1 ton/h. (Fig. 6C). Further improvements in both the plasma and electrolyzer components (e.g., reducing the plasma energy consumption by ~40%, doubling the ammonia yield rates) are expected to reduce the total energy consumption by 46% to 28.0 MWh/t-NH_3 and reduce the LCOA from $5011 to $3453/t-$NH_3$ for its small-scale and distributed deployment (Fig. 6D).

3.3. Reaction mechanism of plasma-electrocatalysis for air-to-NH_3

To unravel the origin of the high performance achieved by plasma-electrocatalysis, a mechanistic understanding of the whole reaction pathway was investigated based on experiments and theoretical simulation (Fig. S21). For the first step of air-to-NH_3 conversion, air activation by rotating gliding arc plasma was analyzed (Fig. 7A). Initiated by the collisions between electrons and air, the energy transferred from electrons to air was estimated via different channels of excitation, ionization and dissociation of N_2 and O_2 determined by the reduced electric field (E/N, where E is electric field and N is the concentration of neutral particles) and electron energy distribution (Table S9) [58]. For our system, the reduced electric field was in the range of 10~100 Td (Fig. S22), and the majority of electrons were at relatively low energies (Fig. S23). This means that electron-impact vibrational excitation of N_2 and O_2 accounts for 50%~90% of electron energy [59]. Thus, electron-induced vibrational excitation of the N_2 bond (N≡N, 948 kJ/mol) and the O_2 bond (O=O, 498 kJ/mol) was estimated to play a significant role in the subsequent reactions, especially the interactions with atomic O and N to produce NO via the non-thermal Zeldovich mechanism (Fig. 7A and Eqs. (2) and (3)). Recent works also confrmed that vibrational excitation can enhance the generation of NO_x [44,58]. For RGA plasma, the vibrational temperature normally can achieve to nearly 4000~5000 K, which implied the strengthen effect of vibrationally excited activation of N_2 in plasma compared with conventional technologies limited by thermal equilibrium [60,61].

$$O + N_{2,vib} \rightarrow NO + N \quad (2)$$

$$N + O_{2,vib} \rightarrow NO + O \quad (3)$$

Due to the interactions between plasma and water vapor, the formations of OH radicals may also contribute to the formation and further delivery of NO_x into the electrolyte [45]. In fact, versatile active species were observed in OES spectrum, such as N_2 second positive systems (SPS), N_2^+ first negative system (FNS), NO (A-X) and O_2 (B-X) as well as OH radicals (A-X) (Table S2). These metastable molecules were prone to involve in heavy particles collision reactions (Table S10). Further oxidation of NO by reaction with O atom was the main route to form NO_2, whereas the loss of NO_2 was via the collision path involving O atom or N atom (Fig. 7A). The concentration and ratio of NO and NO_2 depended on $N_2/O_2/H_2O$ plasma chemistries [59,62–64]. The average NO concentration was ~15000 ppm, with a NO/NO_2 ratio of ~5 at the exit of the plasma system measured by a gas analyzer. By considering the

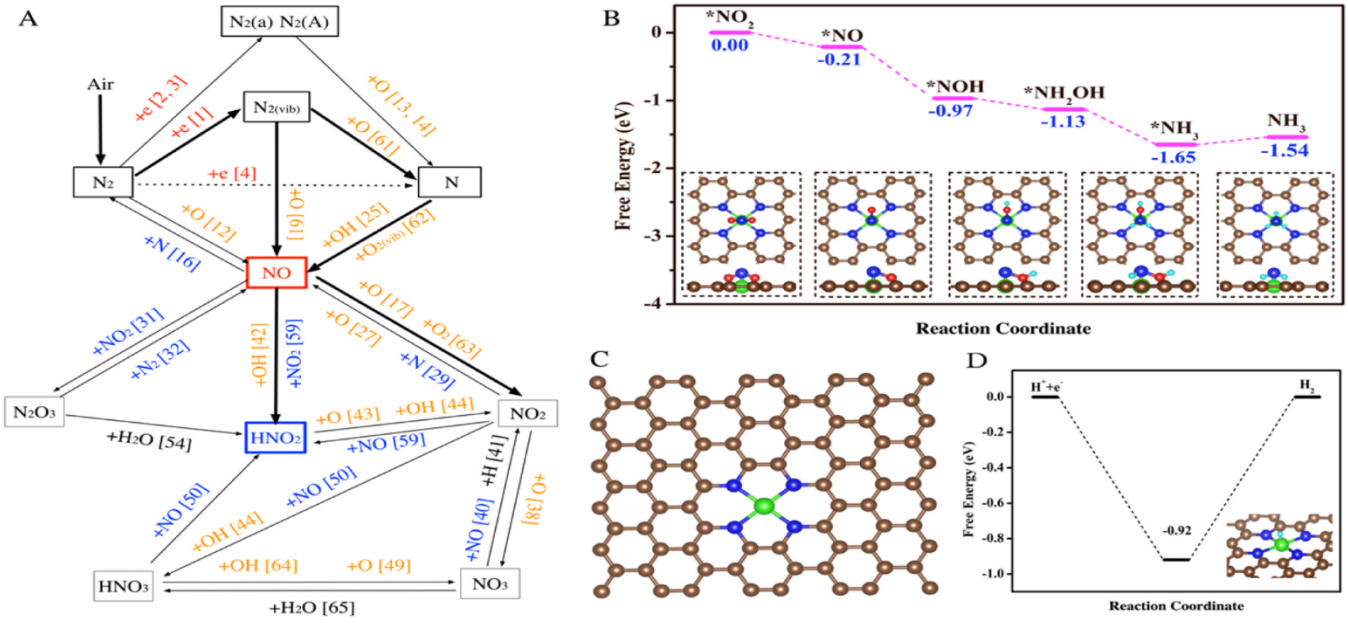

Fig. 7. Plasma chemistry and DFT calculations. (A) Estimated reaction pathways of RNS in NTP (Numbers in brackets indicated the elementary reactions in Supplementary Materials; Thickness of line shows the estimated importance of corresponding reactions). (B) Reaction free profiles for different intermediates from NO_2^- to NH_3. (C) Co SAs/N-C structure. (D) The calculated adsorption energy of H over the surface of Co SAs/N-C.

aforementioned elementary reactions in multi-physical field model, the calculated concentration of NO_2^- was ~0.014 mol/L, which agreed well with the experimental value (~0.015 mol/L) measured by ion chromatography. The concentration of NO_3^- was two orders of magnitude lower than that of NO_2^- (Fig. S24). Based on overall RNS chemistry and product distribution analysis, the main reaction pathway from air to dissolved NO_x intermediaries ($N_2 \rightarrow N_{2(vib)} \rightarrow NO \rightarrow NO_2^-$) was speculated. And this plasma system design provided a relatively energy-efficient and scalable production of gas-phase NO_x (which could be easily converted into nitrite/nitrate) and dissolved NO_2^-. Then, a molecular-level understanding of efficient NH_3 synthesis in plasma-treated electrolyte was obtained by density functional theory (DFT) calculations. According to previous results of ^{15}N isotopic tests and product distribution, NH_3 was produced via a plasma-induced NO_2^- reduction (Figs. S17 and S25). Therefore, the electrochemical reaction ($NO_2^- + 5H_2O + 6e^- \rightarrow NH_3 + 7OH^-$) consisting of a series of deoxidation reactions, $*NO_2^- \rightarrow *NO_2 \rightarrow *NO \rightarrow *N$, followed by hydrogenation reactions, $*N \rightarrow *NH \rightarrow *NH_2 \rightarrow *NH_3$, was calculated to get insight into the process of NH_3 production over Co-N_4 motif with Co atom as the active site (Fig. 4B and C) [49]. The $*NH_3$-to-NH_3 step was the potential-dependent step (PDS), with a maximum free energy of 0.11 eV. Compared to the relatively higher reaction energy of 0.92 eV for HER (Fig. 4D), Co SAs/N-C possessed an increased preference for NO_2^- electroreduction. Overall, we unveiled that the formation of Co-N_4 structure was the origin of high activity and selectivity by facilitating $*NH_3$ desorption and strengthening *H adsorption.

4. Conclusion

Our tandem plasma-electrocatalysis strategy provides an appealing and supplementary alternative to commercial-viable and distributed small-scale nitrogen fixation (Fig. S27). With only ubiquitous air and water as the key reactants, the plasma-electrocatalysis process driven by renewable energy has significant potential to deliver a net-zero emission choice considering the promises of carbon neutrality and on-site NH_3 production. To understand this unique air-to-NH_3 route with four-state (gas-plasma-liquid-solid) matter transformation, in-depth studies of NTP kinetics, electrocatalysis and DFT were performed. Results revealed that electron-induced vibrational excitation promoted air activation, while coordination-modulation of Co SAs/N-C facilitated $*NH_3$ desorption and strengthened *H adsorption. By understanding and optimizing the synergy between the NTP and electrocatalysis, the tandem "plasma-electrocatalysis" strategy using intermittent renewable energy has great potential to open a new route for the synthesis of other important platform chemicals from inert molecules (e.g., CO_2, CH_4…) with strong chemical bonds.

CRediT authorship contribution statement

Wu Angjian, Li Xiaodong: Conceptualization, Writing – original draft. **Wu Angjian, Yangji**: Methodology. **Xu Bo, Wu Xiao-Yu**: Software. **Wang Yuhang, Xingjie Lv, Xu Aoni**: Data curation. **Zheng Jiageng, Tan Qinhuai, Peng Yaqi, Qi Haifeng**: Investigation; **Li Jianfeng, Ma Yichen, Wang Yaolin, Harding Jonathan, Zhifu Qi, Tu Xin**: Writing – review & editing. **Wang Aiqin, Yan Jianhua, Li Xiaodong**: Supervision.

Declaration of Competing Interest

The authors declare that they have no known competing financial interests or personal relationships that could have appeared to influence the work reported in this paper.

Acknowledgements

This work was supported by the National Natural Science Foundation of China (No. 51976191, 51806193). We acknowledge support from Innovative Research Groups of the National Natural Science Foundation of China (No. 51621005), Ecological civilization project, Zhejiang University and the Program of Introducing Talents of Discipline to University (No. BP0820002). X.Y. Wu is supported by the Start-up Grant of University of Waterloo. We also appreciated for the constructive discussion and support from Dr. J Wang from Stanford University, Dr. M Zhang from Hong Kong Polytechnic University and Prof. L Wang from National University of Singapore.

Appendix A. Supporting information

Supplementary data associated with this article can be found in the online version at doi:10.1016/j.apcatb.2021.120667.

References

[1] S.L. Foster, S.I.P. Bakovic, R.D. Duda, S. Maheshwari, R.D. Milton, S.D. Minteer, M. J. Janik, J.N. Renner, L.F. Greenlee, Catalysts for nitrogen reduction to ammonia, Nat. Catal. 1 (2018) 490–500.
[2] H.K. Lee, C.S.L. Koh, Y.H. Lee, C. Liu, I.Y. Phang, X. Han, C.-K. Tsung, X.Y. Ling, Favoring the unfavored: selective electrochemical nitrogen fixation using a reticular chemistry approach, Sci. Adv. 4 (2018), eaar3208.
[3] X. Zi, J. Wan, X. Yang, W. Tian, H. Zhang, Y. Wang, Vacancy-rich 1T-MoS_2 monolayer confined to MoO_3 matrix: an interface-engineered hybrid for efficiently electrocatalytic conversion of nitrogen to ammonia, Appl. Catal. B Environ. 286 (2021), 119870.
[4] P.-Y. Liu, K. Shi, W.-Z. Chen, R. Gao, Z.-L. Liu, H. Hao, Y.-Q. Wang, Enhanced electrocatalytic nitrogen reduction reaction performance by interfacial engineering of MOF-based sulfides $FeNi_2S_4$/NiS hetero-interface, Appl. Catal. B Environ. 287 (2021), 119956.
[5] Q. Wang, J. Guo, P. Chen, Recent progress towards mild-condition ammonia synthesis, J. Energy Chem. 36 (2019) 25–36.
[6] N. Cherkasov, A.O. Ibhadon, P. Fitzpatrick, A review of the existing and alternative methods for greener nitrogen fixation, Chem. Eng. Process. Process Intensif. 90 (2015) 24–33.
[7] C. Zhao, S. Zhang, M. Han, X. Zhang, Y. Liu, W. Li, C. Chen, G. Wang, H. Zhang, H. Zhao, Ambient electrosynthesis of ammonia on a biomass-derived nitrogen-doped porous carbon electrocatalyst: contribution of pyridinic nitrogen, ACS Energy Lett. 4 (2019) 377–383.
[8] J.W. Erisman, M.A. Sutton, J. Galloway, Z. Klimont, W. Winiwarter, How a century of ammonia synthesis changed the world, Nat. Geosci. 1 (2008) 636–639.
[9] G. Soloveichik, Electrochemical synthesis of ammonia as a potential alternative to the Haber–Bosch process, Nat. Catal. 2 (2019) 377–380.
[10] J.G. Chen, R.M. Crooks, L.C. Seefeldt, K.L. Bren, R.M. Bullock, M.Y. Darensbourg, P.L. Holland, B. Hoffman, M.J. Janik, A.K. Jones, M.G. Kanatzidis, P. King, K. M. Lancaster, S.V. Lymar, P. Pfromm, W.F. Schneider, R.R. Schrock, Beyond fossil fuel–driven nitrogen transformations, Science 360 (2018), eaar6611.
[11] X. Xu, X. Tian, B. Sun, Z. Liang, H. Cui, J. Tian, M. Shao, 1 T-phase molybdenum sulfide nanodots enable efficient electrocatalytic nitrogen fixation under ambient conditions, Appl. Catal. B Environ. 272 (2020), 118984.
[12] X. Yang, S. Sun, L. Meng, K. Li, S. Mukherjee, X. Chen, J. Lv, S. Liang, H.-Y. Zang, L.-K. Yan, G. Wu, Molecular single iron site catalysts for electrochemical nitrogen fixation under ambient conditions, Appl. Catal. B Environ. 285 (2021), 119794.
[13] L. Xiao, S. Zhu, Y. Liang, Z. Li, S. Wu, S. Luo, C. Chang, Z. Cui, Effects of hydrophobic layer on selective electrochemical nitrogen fixation of self-supporting nanoporous Mo4P3 catalyst under ambient conditions, Appl. Catal. B Environ. 286 (2021), 119895.
[14] Y. Shi, Y. Liu, Vacancy and N dopants facilitated Ti3+ sites activity in 3D Ti3-xC2Ty MXene for electrochemical nitrogen fixation, Appl. Catal. B Environ. 297 (2021), 120482.
[15] C. Wang, L.-L. Gu, S.-Y. Qiu, J. Gao, Y.-C. Zhang, K.-X. Wang, J.-J. Zou, P.-J. Zuo, X.-D. Zhu, Modulating $CoFe_2O_4$ nanocube with oxygen vacancy and carbon wrapper towards enhanced electrocatalytic nitrogen reduction to ammonia, Appl. Catal. B Environ. 297 (2021), 120452.
[16] A.J. Martín, J. Pérez-Ramírez, Heading to distributed electrocatalytic conversion of small abundant molecules into fuels, chemicals, and fertilizers, Joule 3 (2019) 2602–2621.
[17] X. Li, Y. Luo, Q. Li, Y. Guo, K. Chu, Constructing an electron-rich interface over an Sb/Nb2CTx–MXene heterojunction for enhanced electrocatalytic nitrogen reduction, J. Mater. Chem. A 9 (2021) 15955–15962.
[18] K. Chu, Q.-q Li, Y.-p Liu, J. Wang, Y.-h Cheng, Filling the nitrogen vacancies with sulphur dopants in graphitic C_3N_4 for efficient and robust electrocatalytic nitrogen reduction, Appl. Catal. B Environ. 267 (2020), 118693.
[19] Q. Li, Y. Guo, Y. Tian, W. Liu, K. Chu, Activating VS2 basal planes for enhanced NRR electrocatalysis: the synergistic role of S-vacancies and B dopants, J. Mater. Chem. A 8 (2020) 16195–16202.
[20] K. Chu, Y.-p Liu, Y.-b Li, Y.-l Guo, Y. Tian, Two-dimensional (2D)/2D interface engineering of a MoS_2/C_3N_4 heterostructure for promoted electrocatalytic nitrogen fixation, ACS Appl. Mater. Interfaces 12 (2020) 7081–7090.

[21] R. Hawtof, S. Ghosh, E. Guarr, C. Xu, R. Mohan Sankaran, J.N. Renner, Catalyst-free, highly selective synthesis of ammonia from nitrogen and water by a plasma electrolytic system, Sci. Adv. 5 (2019) 5778 (eaat5778).

[22] X. Cui, C. Tang, Q. Zhang, A review of electrocatalytic reduction of dinitrogen to ammonia under ambient conditions, Adv. Energy Mater. 8 (2018), 1800369.

[23] P. Mehta, P. Barboun, F.A. Herrera, J. Kim, P. Rumbach, D.B. Go, J.C. Hicks, W. F. Schneider, Overcoming ammonia synthesis scaling relations with plasma-enabled catalysis, Nat. Catal. 1 (2018) 269–275.

[24] J. Choi, B.H.R. Suryanto, D. Wang, H.-L. Du, R.Y. Hodgetts, F.M. Ferrero Vallana, D.R. MacFarlane, A.N. Simonov, Identification and elimination of false positives in electrochemical nitrogen reduction studies, Nat. Commun. 11 (2020) 5546.

[25] H. Liu, N. Guijarro, J. Luo, The pitfalls in electrocatalytic nitrogen reduction for ammonia synthesis, J. Energy Chem. 61 (2021) 149–154.

[26] B.S. Patil, N. Cherkasov, J. Lang, A.O. Ibhadon, V. Hessel, Q. Wang, Low temperature plasma-catalytic NOx synthesis in a packed DBD reactor: effect of support materials and supported active metal oxides, Appl. Catal. B Environ. 194 (2016) 123–133.

[27] N. Bouchoul, H. Touati, E. Fourré, J.-M. Clacens, I. Batonneau-Gener, C. Batiot-Dupeyrat, Plasma-catalysis coupling for CH_4 and CO_2 conversion over mesoporous macroporous Al_2O_3: influence of the physico-chemical properties, Appl. Catal. B Environ. 295 (2021), 120262.

[28] X. Pei, D. Gidon, Y.-J. Yang, Z. Xiong, D.B. Graves, Reducing energy cost of NOx production in air plasmas, Chem. Eng. J. 362 (2019) 217–228.

[29] L.R. Winter, J.G. Chen, N_2 fixation by plasma-activated processes, Joule 5 (2021) 300–315.

[30] J. Long, S. Chen, Y. Zhang, C. Guo, X. Fu, D. Deng, J. Xiao, Direct electrochemical ammonia synthesis from nitric oxide, Angew. Chem. Int. Ed. 132 (2020) 9798–9805.

[31] G.-F. Chen, Y. Yuan, H. Jiang, S.-Y. Ren, L.-X. Ding, L. Ma, T. Wu, J. Lu, H. Wang, Electrochemical reduction of nitrate to ammonia via direct eight-electron transfer using a copper–molecular solid catalyst, Nat. Energy 5 (2020) 605–613.

[32] S. Kumari, S. Pishgar, M.E. Schwarting, W.F. Paxton, J.M. Spurgeon, Synergistic plasma-assisted electrochemical reduction of nitrogen to ammonia, Chem. Commun. 54 (2018) 13347–13350.

[33] L. Huang, J. Chen, L. Gan, J. Wang, S. Dong, Single-atom nanozymes, Sci. Adv. 5 (2019), eaav5490.

[34] C. Choi, S. Back, N.-Y. Kim, J. Lim, Y.-H. Kim, Y. Jung, Suppression of hydrogen evolution reaction in electrochemical N_2 reduction using single-atom catalysts: a computational guideline, ACS Catal. 8 (2018) 7517–7525.

[35] F.W. Boyom-Tatchemo, F. Devred, G. Ndiffo-Yemeli, S. Laminsi, E.M. Gaigneaux, Plasma-induced redox reactions synthesis of nanosized α-, γ- and δ-MnO_2 catalysts for dye degradation, Appl. Catal. B Environ. 260 (2020), 118159.

[36] C. Tang, S.-Z. Qiao, How to explore ambient electrocatalytic nitrogen reduction reliably and insightfully, Chem. Soc. Rev. 48 (2019) 3166–3180.

[37] W. Kohn, L.J. Sham, Self-consistent equations including exchange and correlation effects, Phys. Rev. 140 (1965) A1133–A1138.

[38] P. Giannozzi, S. Baroni, N. Bonini, M. Calandra, R. Car, C. Cavazzoni, D. Ceresoli, G.L. Chiarotti, M. Cococcioni, I. Dabo, QUANTUM ESPRESSO: a modular and open-source software project for quantum simulations of materials, J. Phys. Condens. Matter Inst. Phys. J. 21 (2009), 395502.

[39] J.P. Perdew, Y. Wang, Accurate and simple analytic representation of the electron-gas correlation energy, Phys. Rev. B 45 (1992) 13244–13249.

[40] N. Troullier, J.L. Martins, Efficient pseudopotentials for plane-wave calculations, Phys. Rev. B 43 (1991) 1993–2006.

[41] H.J. Monkhorst, J.D. Pack, Special points for Brillouin-zone integrations, Phys. Rev. B 13 (1976) 5188–5192.

[42] L. Wang, M. Xia, H. Wang, K. Huang, C. Qian, C.T. Maravelias, G.A. Ozin, Greening ammonia toward the solar ammonia refinery, Joule 2 (2018) 1055–1074.

[43] H. Chen, A. Wu, S. Mathieu, P. Gao, X. Li, B.Z. Xu, J. Yan, X. Tu, Highly efficient nitrogen fixation enabled by an atmospheric pressure rotating gliding arc, Plasma Process. Polym. 18 (2021), 2000200.

[44] F. Jardali, S. Van Alphen, J. Creel, H. Ahmadi Eshtehardi, M. Axelsson, R. Ingels, R. Snyders, A. Bogaerts, NOx production in a rotating gliding arc plasma: potential avenue for sustainable nitrogen fixation, Green Chem. 23 (2021) 1748–1757.

[45] J. Sun, D. Alam, R. Daiyan, H. Masood, T. Zhang, R. Zhou, P.J. Cullen, E.C. Lovell, A. Jalili, R. Amal, A hybrid plasma electrocatalytic process for sustainable ammonia production, Energy Environ. Sci. 14 (2021) 865–872.

[46] A. Lindsay, C. Anderson, E. Slikboer, S. Shannon, D. Graves, Momentum, heat, and neutral mass transport in convective atmospheric pressure plasma-liquid systems and implications for aqueous targets, J. Phys. D Appl. Phys. 48 (2015), 424007.

[47] S. Liu, H. Yang, X. Huang, L. Liu, W. Cai, J. Gao, X. Li, T. Zhang, Y. Huang, B. Liu, Identifying active sites of nitrogen-doped carbon materials for the CO_2 reduction reaction, Adv. Funct. Mater. 28 (2018), 1800499.

[48] J. Li, S. Ghoshal, W. Liang, M.-T. Sougrati, F. Jaouen, B. Halevi, S. McKinney, G. McCool, C. Ma, X. Yuan, Z.-F. Ma, S. Mukerjee, Q. Jia, Structural and mechanistic basis for the high activity of Fe–N–C catalysts toward oxygen reduction, Energy Environ. Sci. 9 (2016) 2418–2432.

[49] W. Liu, L. Zhang, W. Yan, X. Liu, X. Yang, S. Miao, W. Wang, A. Wang, T. Zhang, Single-atom dispersed Co–N–C catalyst: structure identification and performance for hydrogenative coupling of nitroarenes, Chem. Sci. 7 (2016) 5758–5764.

[50] L. Cao, Q. Luo, W. Liu, Y. Lin, X. Liu, Y. Cao, W. Zhang, Y. Wu, J. Yang, T. Yao, S. Wei, Identification of single-atom active sites in carbon-based cobalt catalysts during electrocatalytic hydrogen evolution, Nat. Catal. 2 (2019) 134–141.

[51] Y. Zhao, R. Shi, X. Bian, C. Zhou, Y. Zhao, S. Zhang, F. Wu, G.I.N. Waterhouse, L.-Z. Wu, C.-H. Tung, T. Zhang, Ammonia detection methods in photocatalytic and electrocatalytic experiments: how to improve the reliability of NH3 production rates? Adv. Sci. 6 (2019), 1802109.

[52] Y. Gorbanev, E. Vervloessem, A. Nikiforov, A. Bogaerts, Nitrogen fixation with water vapor by nonequilibrium plasma: toward sustainable ammonia production, ACS Sustain. Chem. Eng. 8 (2020) 2996–3004.

[53] X. Xue, R. Chen, C. Yan, P. Zhao, Y. Hu, W. Zhang, S. Yang, Z. Jin, Review on photocatalytic and electrocatalytic artificial nitrogen fixation for ammonia synthesis at mild conditions: advances, challenges and perspectives, Nano Res. 12 (2019) 1229–1249.

[54] A. Liu, Y. Yang, X. Ren, Q. Zhao, M. Gao, W. Guan, F. Meng, L. Gao, Q. Yang, X. Liang, T. Ma, Current progress of electrocatalysts for ammonia synthesis through electrochemical nitrogen reduction under ambient conditions, ChemSusChem 13 (2020) 3766–3788.

[55] A.J. Martín, T. Shinagawa, J. Pérez-Ramírez, Electrocatalytic reduction of nitrogen: from haber-bosch to ammonia artificial leaf, Chem 5 (2019) 263–283.

[56] G. Hochman, A.S. Goldman, F.A. Felder, J.M. Mayer, A.J.M. Miller, P.L. Holland, L. A. Goldman, P. Manocha, Z. Song, S. Aleti, Potential economic feasibility of direct electrochemical nitrogen reduction as a route to ammonia, ACS Sustain. Chem. Eng. 8 (2020) 8938–8948.

[57] E. Vervloessem, M. Aghaei, F. Jardali, N. Hafezkhiabani, A. Bogaerts, Plasma-based N_2 fixation into NOx: insights from modeling toward optimum yields and energy costs in a gliding arc plasmatron, ACS Sustain. Chem. Eng. 8 (2020) 9711–9720.

[58] W. Wang, B. Patil, S. Heijkers, V. Hessel, A. Bogaerts, Nitrogen fixation by gliding arc plasma: better insight by chemical kinetics modelling, ChemSusChem 10 (2017) 2145–2157.

[59] Y. Ohmori, M. Shimozuma, H. Tagashira, Boltzmann equation analysis of electron swarm behaviour in nitrogen, J. Phys. D Appl. Phys. 21 (1988) 724–729.

[60] A.J. Wu, H. Zhang, X.D. Li, S.Y. Lu, C.M. Du, J.H. Yan, Determination of spectroscopic temperatures and electron density in rotating gliding arc discharge, IEEE Trans. Plasma Sci. 43 (2015) 836–845.

[61] A. Wu, J. Yan, H. Zhang, M. Zhang, C. Du, X. Li, Study of the dry methane reforming process using a rotating gliding arc reactor, Int. J. Hydrog. Energy 39 (2014) 17656–17670.

[62] W. Van Gaens, A. Bogaerts, Corrigendum: kinetic modelling for an atmospheric pressure argon plasma jet in humid air (2013 J. Phys. D: Appl. Phys. 46 275201), J. Phys. D Appl. Phys. 47 (2014), 079502.

[63] P. Lukes, E. Dolezalova, I. Sisrova, M. Clupek, Aqueous-phase chemistry and bactericidal effects from an air discharge plasma in contact with water: evidence for the formation of peroxynitrite through a pseudo-second-order post-discharge reaction of H_2O_2 and HNO_2, Plasma Sources Sci. Technol. 23 (2014), 015019.

[64] Y. Wang, A. Xu, Z. Wang, L. Huang, J. Li, F. Li, J. Wicks, M. Luo, D.-H. Nam, C.-S. Tan, Y. Ding, J. Wu, Y. Lum, C.-T. Dinh, D. Sinton, G. Zheng, E.H. Sargent, Enhanced nitrate-to-ammonia activity on copper–nickel alloys via tuning of intermediate adsorption, J. Am. Chem. Soc. 142 (2020) 5702–5708.